System-Level Simulation Suite for the Design of mmWave-Over-Fiber-Based Distributed Antenna Systems

Arno Moerman, *Student Member, IEEE*, Olivier Caytan, *Member, IEEE*, Laura Van Messem, *Student Member, IEEE*, Joris Van Kerrebrouck, *Member, IEEE*, Guy Torfs, *Senior Member, IEEE*, Piet Demeester, *Fellow, IEEE*, Hendrik Rogier, *Senior Member, IEEE*, and Sam Lemey, *Member, IEEE*

***Abstract*— Although challenging propagation conditions reduce its reliability, the mmWave spectrum is considered a cornerstone of (beyond-)5G networks. Recently, distributed antenna systems (DASs) surrounding the mobile users with multiple remote antenna units (RAUs) interconnected by mmWave-over-fiber technology were identified as a prime candidate to unlock high throughput and reliable coverage. This article proposes a dedicated simulation suite facilitating the deployment of such a mmWave-over-fiber-based DAS by accurately predicting system-level performance and enabling time-efficient optimization of the hardware configuration, including the RAUs, the central office (CO), and the signal processing units, toward the target application. It incorporates accurate models for the mmWave-over-fiber link and the amplifiers, including nonlinear distortion and noise, full-wave electromagnetic models for the antenna front-ends, and analytical models for the wireless channel. The simulation suite is validated by a measurement campaign, not only focusing on a single mobile user served by a fixed-beam RAU but also considering a multibeam RAU serving two users simultaneously by means of two independent mmWave-over-fiber links. The model accurately predicts up- and downlink quality over a wide range of user positions, different system parameters, and also accurately captures inter-user interference.**

***Index Terms*— Air-filled substrate-integrated waveguide (AFSIW), Butler matrix, corporate-feed array, distributed antenna system (DAS), mmwave-over-fiber, radio frequency-over-fiber (RFoF), system-level model.**

Manuscript received 15 November 2022; revised 10 February 2023 and 29 March 2023; accepted 4 April 2023. This work was supported in part by the Methusalem Funding of the Flemish Government under Grant "SHAPE: Next Generation Wireless Networks" and in part by the European Research Council through "ATTO: A New Concept for Ultrahigh Capacity Wireless Networks" under Grant 695495. This paper is an expanded version from the 2022 IEEE International Symposium on Phased Array Systems and Technology (Array 2022), Waltham, MA, USA, October 11–14, 2022 [DOI: 10.1109/PAST49659.2022.9975041]. *(Corresponding author: Arno Moerman.)*

The authors are with the Department of Information Technology, Ghent University/imec, 9052 Ghent, Belgium (e-mail: arno.moerman@ugent.be; olivier.caytan@ugent.be; laura.vanmessem@ugent.be; joris.vankerrebrouck@ugent.be; guy.torfs@ugent.be; piet.demeester@ugent.be; hendrik.rogier@ugent.be; sam.lemey@ugent.be).

Color versions of one or more figures in this article are available at https://doi.org/10.1109/TMTT.2023.3267545.

Digital Object Identifier 10.1109/TMTT.2023.3267545

I. Introduction

THE coming generations of mobile networks aim to realize the Internet of Everything (IoE), providing a large number of users and devices high-performance wireless access well beyond the capabilities of current 5G networks [1] in terms of throughput, latency, and reliability. In combination with the congestion of the sub-6 GHz band, these ambitious performance requirements are the driving forces behind the ongoing trend toward the mmWave (30–300 GHz) and terahertz (0.1–10 THz) frequency bands, where there is still an abundance of unexploited spectrum. Yet, this shift directly entails a more challenging propagation environment due to more pronounced shadowing, higher penetration losses, and increased path loss. Fortunately, by integrating multiple antennas in an array, the aforementioned obstacles can be mitigated by adopting adaptive beamforming techniques. In addition, the accompanying increase in directivity enables more stable wireless channels by filtering out multipath components. Yet, a conventional co-located antenna array approach is still susceptible to non-line-of-sight (NLoS) blockage [2] when a static or dynamic blocker is in the direct path between the base station and the user equipment (UE).

Recently, several innovative concepts have been proposed to maintain high-data-rate wireless connectivity in challenging NLoS situations. One approach consists in distributing active, intentional reflectors in the UE's environment to intelligently scatter the incident fields [3], [4], [5] around the obstacle. These reflectors can either be phased-array-based relays [3], which retransmit an amplified version of the signal, or intelligent reflective surfaces (IRSs) [5], which alter the propagation direction of the incident wave. Another solution [2] leverages a distributed antenna system (DAS) where several remote antenna units (RAUs) are strategically deployed in the environment of the UE. Even with a limited number of RAUs, the probability of maintaining a line-of-sight (LoS) path between the UE and the DAS increases significantly [6], [7]. By massively increasing the number of radiating elements, the UE can be located in the near-field of the entire system, approaching the concept of a large intelligent

surface (LIS) [8], enabling unprecedented energy focusing in a confined volume and minimizing inter-user interference. In [2] and [9], a mmWave DAS is proposed that leverages mmWave-over-fiber to efficiently exchange broadband mmWave signals between the central office (CO) and distributed RAUs. In contrast to intermediate-frequency-over-fiber (IFoF) [10], which distributes the intermediate-frequency signal and a local oscillator (LO) signal, mmWave-over-fiber directly distributes the mmWave signals, thereby simplifying the RAU's architecture by omitting mixers, at the cost of needing high-speed electro-optic components. Moreover, mmWave-over-fiber ensures tight synchronization between all mixer-free RAUs, paving the way for distributed beamforming and distributed multi-input multi-output (DMIMO) [6], [11]. An extensive measurement campaign has proven that such a mmWave-over-fiber DAS is able to achieve reliable communication with data rates up to 48 Gb/s in a harsh realistic indoor environment with NLoS conditions [2]. However, [2], [9], and [12] also showed that a mmWave-over-fiber DAS requires custom tailoring to the deployment environment, including judicious optimization of the required amplification level at various nodes in the opto-electronic transmit/receive (TRX) chain to obtain maximum wireless performance.

Despite many measurements [2], [9], [12] and models [13], [14], [15], [16], [17], [18] being found in literature, a system-level model for the evaluation and design of mmWave-over-fiber-based fiber-wireless (FiWi) down- and uplinks has so far been missing, making accurate and complete analysis very challenging and hindering the deployment on a large scale. Dedicated models in literature focus either on the radio equipment [13] or on the optical components [15], [16], [17], [18]. In [15], a rigorous expression for an analog radio-over-fiber link is presented to study the amplitude and phase of the detected signal's fundamental frequency and its harmonics for different optical modulation formats. Furthermore, Cox et al. [16] analyze the fundamental limits of intrinsic mmWave-over-fiber links and compare the state-of-the-art opto-electric components with these limits to acquire insight into the limitations of the fiber link in a mmWave-over-fiber-based DAS. Tian et al. [18] combine an analytical model with simulations in a visual programming interface (VPI) transmission maker for a mmWave-over-fiber link between CO and RAU to study the signal quality for different received powers at the RAU. James et al. [19] study the signal quality of a WiMax signal in a mmWave-over-fiber wireless downlink and verify the measurement results with the simulations in VPI Photonics. Although it is very important to keep these limitations in mind when designing the mmWave-over-fiber wireless link, it is also of major importance to incorporate the mmWave wireless channel and the imperfections of additional active front-end components, essential to combat the high propagation losses. This is also confirmed in [20], pinpointing the mmWave radio as the main source of degradation, rather than the optical link, after in-depth characterization of the nonlinear behavior of a single FiWi end-to-end link.

In this article, we propose a versatile and time-efficient system-level simulation suite to accurately predict and optimize the down- and uplink signal quality of a mmWave-over-fiber-based DAS. It includes the nonlinear behavior of all the active electronic components and opto-electronic transducers, while also incorporating antenna system imperfections and the wireless channel between RAU and UE. Moreover, the simulation suite allows to study the influence of several active components on the link quality. The proposed model enables fast optimization of the mmWave-over-FiWi link between CO and UE while providing more insight into the system's bottlenecks and the signal quality at different stages in the link. This article is an invited extension of our work presented at the PAST2022 conference [21]. This article now describes the simulation suite (architecture, inputs/outputs, and interfaces) in more detail and extends the conference contribution to multibeam multiuser support. Moreover, to validate the simulation suite and prove its versatility, a wide range of measurement scenarios are analyzed, including uplink communication, different wireless channels, and an alternative RAU configuration with local beamforming [22].

This work is organized as follows. Sections II-A and II-B introduce the concept of a mmWave DAS and elaborate on a mmWave-over-fiber wireless link, respectively. Section II-C introduces the proposed simulation suite by outlining its architecture and defining its interfaces and describes a representative FiWi link to illustrate how our simulation suite can be used. Sections III and IV validate the simulation suite with an extensive measurement campaign. The former examines the case where a fixed-beam 1×4 antenna array with corporate feed is deployed at the RAU, while the latter focuses on a multibeam four-element antenna array Butler matrix serving two UEs. Section V concludes the article.

II. Distributed Antenna System

A. System Overview

To alleviate the challenging propagation environment at mmWave frequencies, the use of a mmWave-over-fiber-based DAS is advocated in [2]. Whereas the DAS ensures reliable mmWave wireless communication, the mmWave-over-fiber architecture provides a low-loss and broadband connection between a CO and several RAUs. In addition, synchronization between different RAUs is ensured owing to the up- and downconversion of the mmWave signals at the CO, while the optical-fiber-based routing ensures immunity to electromagnetic interference (EMI) issues.

Fig. 1 provides a schematic overview of a general mmWave DAS architecture with its main components, being the CO, RAUs, and UE. All signal processing is centralized at the CO, which also houses the mmWave-over-fiber transceivers, each consisting of an electro-optical (E/O) converter for the wireless downlink and an opto-electrical (O/E) converter for the wireless uplink. The RAUs are distributed in the UEs' environment. Owing to the mmWave-over-fiber scheme, the RAUs exhibit low hardware complexity and low power consumption. Therefore, they are highly cost-effective when compared with RAUs tailored toward other optical signal distribution techniques, such as digitized-radio-over-fiber (DRoF) and IFoF [23]. In particular, the RAU only entails O/E and E/O conversion with the

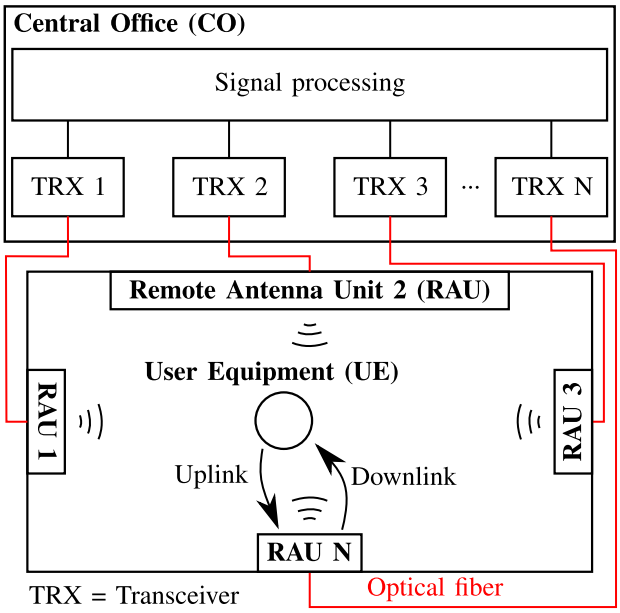

Fig. 1. Schematic overview of a mmWave-over-fiber DAS. The CO implements all signal processing and mmWave-over-fiber transceivers. Strategic distribution of RAUs in the UE's environment ensures LoS communication, while their tight synchronization enables DMIMO schemes.

corresponding electrical amplification and incorporation of a suitable multiantenna system with optional local beamforming. Recently, several high-performance antenna arrays have been proposed in literature that are suitable for integration within a RAU [22], [24], [25]. In addition, since the broadband RF signals are optically distributed to the RAUs, the mmWave-over-fiber architecture facilitates the application of optical beamforming networks (BFNs), offering significant advantages over classical electronic beamforming in terms of insertion loss, bandwidth, and EMI immunity [25], [26] at the expense of more O/E and E/O transducers. To guarantee high-throughput mmWave coverage for the UEs in the presence of mobile blockers, several strategies can be adopted, varying in degree of signal processing complexity. First, the system can switch to the RAU with the best link, allowing maximum hardware reuse [9]. Furthermore, leveraging the inherent synchronization between the RAUs, the DAS can also apply DMIMO, or even holographic beamforming when the number of RAUs is large enough [8]. The latter enables unprecedented energy focusing in a confined volume while also lowering interference to other UEs. Finally, a hybrid approach is also possible.

It can be concluded that to obtain maximum performance, the number of RAUs, their antenna configuration, the signal processing strategy, and the hardware at the CO require careful tailoring toward the targeted application, the wireless propagation environment, and the number of expected UEs. A simulation suite predicting system-level performance is therefore an indispensable tool in rolling out such a DAS.

B. mmWave-over-fiber wireless Link

High-performance mmWave-over-fiber wireless links are vital to the operation of the DAS. Fig. 2(a) shows a representative downlink implementation of such a mmWave-over-fiber wireless link. For every downlink in the system, the mmWave signals are generated and converted into the optical domain at the CO. To this end, a polarization-dependent Mach–Zehnder modulator (MZM), an accompanying polarization controller, and a laser source are used. The MZM is quadrature-biased, where the electrical field of the light carrier is then modulated by the mmWave signals as [27], [28]

$$E_{\text{opt,out}} = E_{\text{opt,in}} \cdot \cos\left(\frac{\pi}{2} \cdot \frac{V_{\text{mmWave}}}{V_\pi} - \frac{\pi}{4}\right) \tag{1}$$

with $E_{\text{opt,out}}$ and $E_{\text{opt,in}}$ being the outgoing and incident optical fields of the MZM, respectively, V_π being the device-specific switching voltage, and V_{mmWave} being the differential voltage driving the MZM. The E/O conversion in the MZM generates a double-sideband (DSB) signal around the light carrier [10]. This signal arrives at the RAU after propagation through a single-mode fiber. Due to inevitable fiber chromatic dispersion and optical DSB modulation, the fiber is limited in length to avoid signal degradation [29]. Nevertheless, this limitation can be overcome to a large extent by adopting optical single sideband (OSSB) modulation [12]. At the RAU, a photodiode performs O/E conversion, generating a photocurrent I_{PD} that only depends on the incident optical power $P_{\text{opt,PD}}$ and the photodiode's responsivity R_{PD}

$$I_{\text{PD}} = R_{\text{PD}} \cdot P_{\text{opt,PD}}. \tag{2}$$

The combination of the MZM biased at quadrature and the photodiode ensures a linear electric back-to-back conversion when the MZM's peak driving voltage is small enough in comparison to the switching voltage V_π of the MZM. As discussed in more detail in [16], note that the electrical back-to-back conversion can have a positive or a negative gain, depending on the laser power and switching voltage V_π, among others [16]. In this article, the same convention is used where a negative gain corresponds to loss. After the optical link, amplifiers are used to increase the signal level and directly drive a BFN, which applies the correct phases and amplitudes to the antenna array elements. Finally, after propagation over the wireless channel, the UE amplifies the received signal again before further processing.

The architecture and system-level model of a potential mmWave-over-FiWi uplink implementation are shown in Fig. 2(d) and (e), respectively. Now, the uplink signal is generated at the UE and processed in the CO. Furthermore, the MZM and the photodiode are placed at the RAU and the CO, respectively. Moreover, the MZM is now driven by a single-ended amplifier. In addition, the laser remains at the CO to further ensure centralization of all expensive hardware [30], and two fibers are used. One fiber transports the optical carrier from CO to RAU, while another fiber returns the modulated light to the CO. While Fig. 2(a) and (d) present the general concept of a mmWave-over-FiWi link, depending on the practical implementation, a single fiber might suffice for both up- and downlink in a time division duplex scheme [12].

C. Simulation Suite

Fig. 3 shows a schematic overview of the system-level simulation suite to analyze mmWave-over-fiber-based

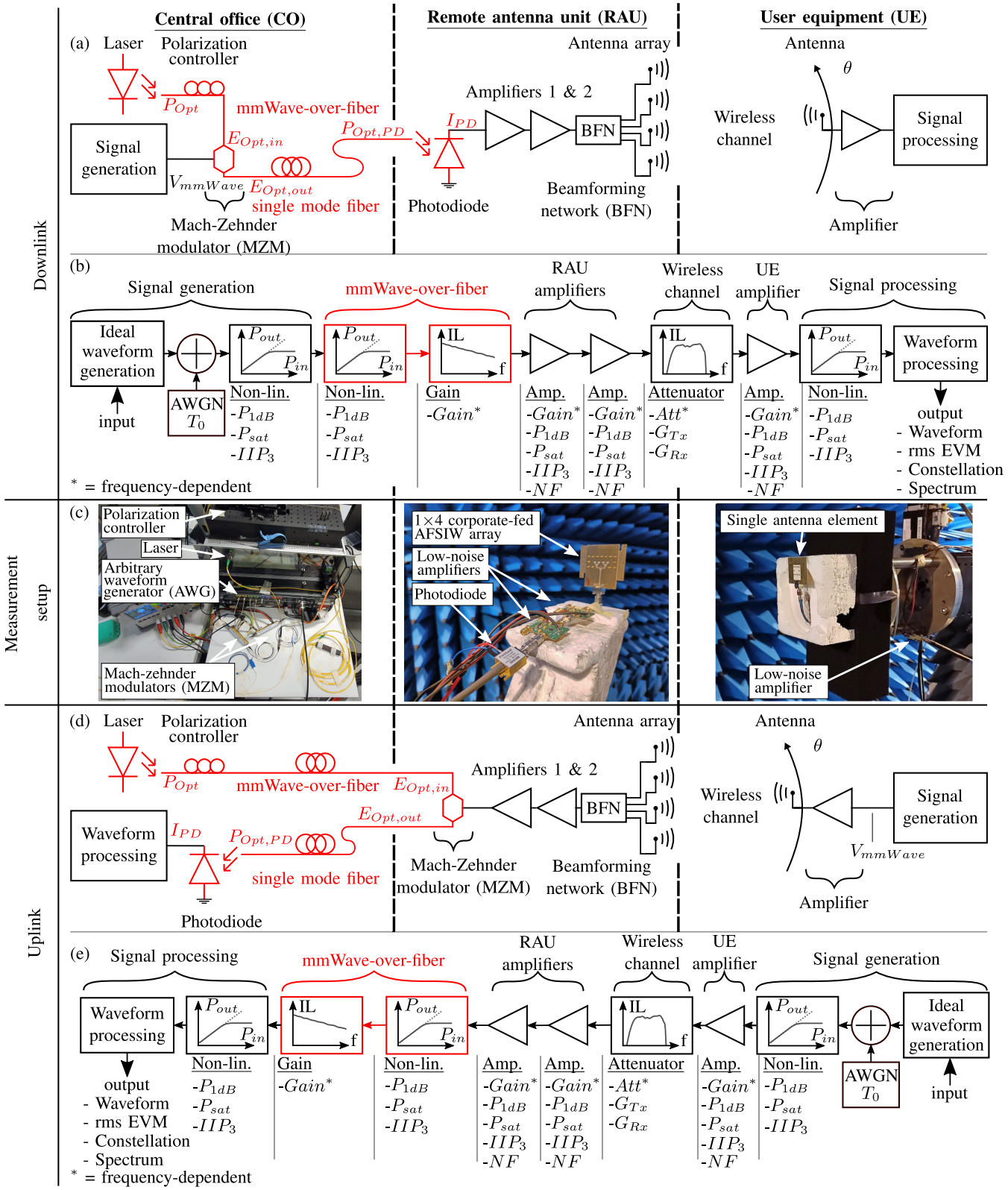

Fig. 2. mmWave-over-fiber wireless down- and uplink consisting of the CO (left), the RAU (middle), and the UE (right). For downlink communication, an MZM performs E/O conversion at the CO, directly modulating the optical carrier with the mmWave signal. After propagation through a single-mode fiber, the signal is converted back into the electrical domain by a photodiode and is amplified to directly drive a BFN with integrated antenna array. The antenna system at the UE receives the signal and amplifies it before processing. Architecture of (a) downlink and (d) and uplink. System-level model overview of (b) downlink and (e) uplink. (c) Measurement setup.

DASs, leveraging component-level models implemented in MATLAB, Keysight SystemVue, CST Microwave Studio, and the Keysight PathWave 89600 VSA software. A main MATLAB script orchestrates the simulation suite by

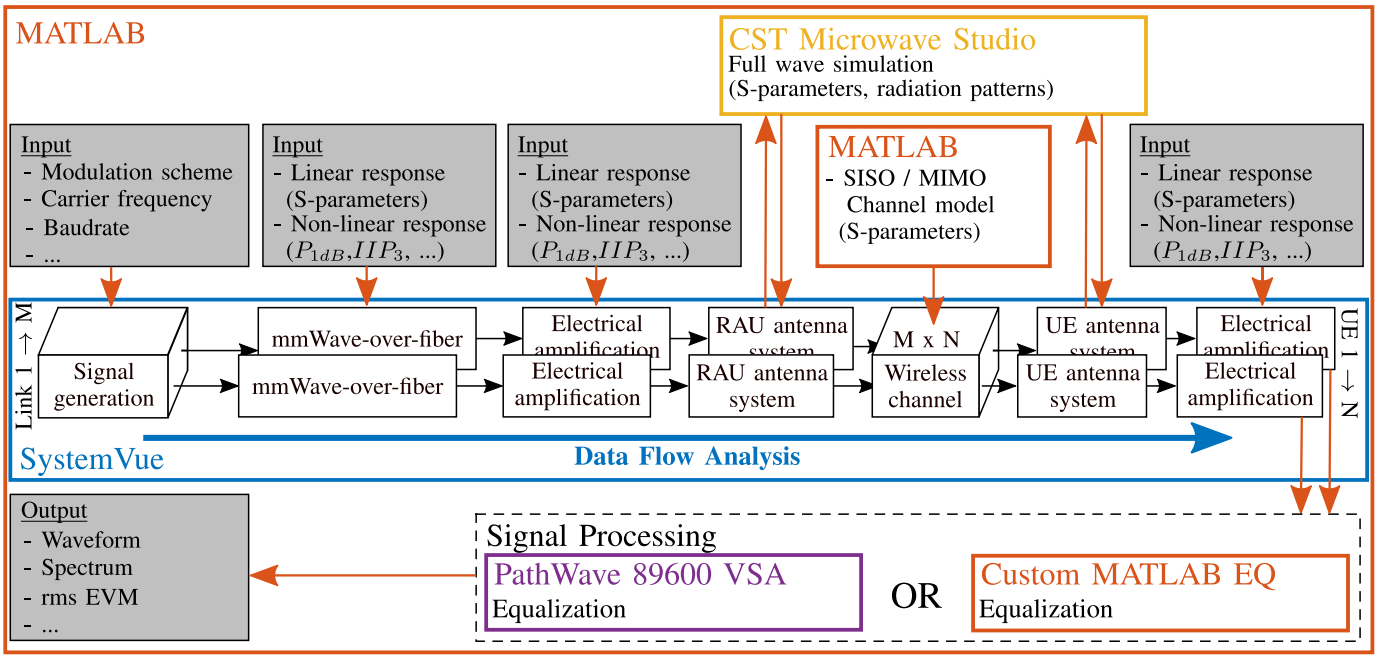

Fig. 3. Schematic overview of the system-level simulation suite: MATLAB dynamically links all software packages and controls the inputs of SystemVue, which simulates the implemented mmWave-over-Fiber DAS. The antenna systems at the RAU and UE are simulated using CST Microwave Studio. A channel model is implemented in MATLAB. Alternatively, measured radiation patterns/channels and other channel models (e.g., obtained via a raytracing tool) can also be imported. SystemVue's Data Flow Analysis calculates the received signals, which can be equalized by either a custom equalizer in MATLAB or PathWave VSA 89500 software.

controlling the different software packages and interfacing them, handling the different inputs and outputs of the different blocks in the simulation suite. At the heart of the simulation suite, Keysight SystemVue is used to generate the waveforms at CO and UEs, and to flexibly model a mmWave-over-fiber-based wireless system architecture. The software's Data Flow Analysis performs a time-domain simulation of the generated waveforms through the model. In the case of a mmWave-over-fiber DAS, this architecture consists of M mmWave-over-fiber links connecting to the M RAUs, N UEs, and a wireless channel describing the propagation environment between the M RAUs and the N UEs. For the signal generation, MATLAB provides several inputs to SystemVue, including the modulation scheme, carrier frequency, baud rate, and the matched filter roll-off factor. Furthermore, it is also possible to incorporate custom (precoded) data to simulate an MIMO system. The other building blocks are characterized by a linear response (consisting of scattering parameters), a nonlinear response (consisting of, e.g., P_{sat}, $P_{1\,\text{dB}}$, IIP_3), or a noise figure (NF), or, in most cases, a combination of these three. A more detailed description of each of the building blocks and their configuration is given below when describing a representative FiWi architecture (Fig. 2) as an application example. These parameters can be found in the datasheet of the component, or obtained via measurements/simulations. In particular, to accurately describe the antenna system at the RAUs and UEs, MATLAB initiates CST Microwave Studio's full-wave solver (if these results are not already present) to obtain their realized gain patterns and S-parameters. Alternatively, when desired, the antenna systems at the RAUs and UE can be modeled by means of measurement data.

The latter are then combined in MATLAB with an appropriate channel model, and provided to SystemVue as a scattering parameter matrix. Alternatively, a measured channel, including antenna effects, could be used. Subsequently, the Data Flow Analysis calculates the signals at the output of each of the UEs, after which they are equalized by either PathWave's VSA 89600 software or a custom equalizer implemented in MATLAB. Finally, based on these equalized waveforms, all the relevant output parameters can be derived, such as the received spectrum and the root-mean-square (rms) error vector magnitude (EVM). By adopting such a modular approach, the simulation suite can be used for a wide variety of use cases, such as the optimization of individual components, while studying their impact on the FiWi link, investigating the performance gain by adopting a co-design approach instead of a more conventional diakoptic approach, analyzing the impact of different local beam steering techniques [22], [25], [31], and testing/verifying different signal algorithms. When combining the proposed simulation suite with appropriate ray-tracing software in the future, it could even be used to optimize the placement of RAUs in a real-life scenario.

Fig. 2(a) shows a representative example of a FiWi downlink, consisting of a RAU serving a single mobile user by means of a beamforming antenna array. The corresponding system-level model in our simulation suite is shown in Fig. 2(b) and consists of a chain of several components, subdivided into different submodels, being the signal generation stage, the mmWave-over-fiber link, the RAU amplifier chain, the wireless channel, the UE amplifier chain, and the signal processing stage. Apart from the signal generation and processing stages, all the components

introduce nonlinear distortion, add white Gaussian noise, or introduce frequency-dependent gain/attenuation. Nonlinear distortion is specified by the input 1-dB compression point ($IIP_{1\,dB}$), the input saturation power (IP_{sat}), and the input third-order intercept point (IIP_3). The amplifiers combine several of these behaviors, introducing nonlinear distortion referred to the output power ($OP_{1\,dB}$/OP_{sat}/OIP_3), applying frequency-dependent gain, and also adding white Gaussian noise, specified by its NF.

In the signal generation submodel, the ideal mmWave signal is combined with additive white Gaussian noise (AWGN), which is characterized by a noise temperature T_0 and serves as an equivalent noise source, aggregating several other noise sources present in the FiWi link. These include not only electronic noise contributions introduced by nonideal signal generation (quantization noise and clock jitter) but also the optical noise sources, such as the shot noise of the photodiode. When using a single-mode laser with a low relaxation frequency and directly driving an MZM, the optical link noise is dominated by the shot noise of the photodiode [32], and the relative intensity noise (RIN) of the laser can be neglected, as in [32]. Yet, if needed, the RIN noise could be incorporated in our simulation suite by adequately modifying the equivalent AWGN noise source [Fig. 2(b) and (e)]. Finally, nonlinear distortion is applied to the noisy mmWave signal, modeling imperfections related to the signal generation with practical digital-to-analog converters (DACs) [33].

The next submodel represents the mmWave-over-fiber link, which consists of the biased MZM, the optical fiber, and the photodiode. The linear behavior of such a unilateral electrical two-port can be described by an $S_{21,\mathrm{opt}}$ scattering parameter, taking into account several frequency-dependent effects such as optical loss and device parasitics. Furthermore, the link's $S_{21,\mathrm{opt}}$ parameter description can be acquired through either simulations or measurements. It depends on several parameters, including the used optical power, influencing the MZM's slope efficiency [16], the MZM's bias voltage [27] and the photodetector's responsivity. Finally, the mmWave-over-fiber submodel also includes the nonlinear distortion introduced by the MZM's E/O conversion, as described by (1).

Next, the model in Fig. 2(b) includes a cascade of components representing the RAU's transmit amplifier chain, the wireless channel, and the UE's receive amplifier chain. Similar to the mmWave-over-fiber link, the wireless channel, which also includes the antenna array and BFN at the RAU and the receive antenna at the UE, is modeled by an S_{21} scattering parameter. Again, the exact description can be generated through either numerical/analytical models or measurements and depends on several parameters, being the propagation environment, the RAU's BFN implementation and configuration, and the positions, orientations, and realized gain patterns G_{RAU} and G_{UE} of the antennas at the RAU and UE.

At the final signal processing stage, a nonlinear distortion component accounts for the imperfections arising from measurement equipment based on practical analog-to-digital converters (ADCs). The waveform processing demodulates and potentially equalizes the received signal and calculates the rms EVM as a figure of merit, which is a metric for the difference between the received and ideal constellation points. Based on the criteria by 3GPP, EVM values below 17.5%, 12.5%, and 8% allow transmission of quaterny phase-shift keying (QPSK), quadratic-amplitude modulation (16-QAM), or 64-QAM symbols, respectively, giving an indication of achievable data rates [34].

Similarly, a representative model for the uplink is shown in Fig. 2(e), consisting of similar submodels, yet in a different order, showing the flexibility of the proposed simulation suite.

III. Antenna Array With Corporate Feed

As a validation of the proposed model, we consider the case of a DAS with a single RAU based on the antenna array with corporate feed proposed in [24]. First, the influence of several system parameters on the signal quality, quantified in terms of the rms EVM, will be investigated and compared with the measurements. The studied parameters are the RF power, optical power, and symbol rate. In addition, the downlink EVM is predicted as a function of UE position in the room. For a given cross section in this room, the result of the model is compared with the measurements for both the downlink and the uplink. Moreover, a two-ray ground-reflection propagation channel model is implemented in MATLAB to show the versatility of the simulation suite. In this case, the measured received spectrum and constellation at the UE are compared with the simulation suite's predictions.

A. Measurement Setup and System-Level Model Parameters

In Fig. 2(c), an annotated picture is shown of the CO, RAU, and UE of the deployed DAS. In the setup, a fixed-beam 1 × 4 air-filled substrate-integrated waveguide (AFSIW) antenna array with corporate feed [24] is used at the RAU, while a single AFSIW antenna element is used at the UE. The individual antennas exhibit a peak gain of 7.4 dBi and an efficiency of at least 85% in the [24.25–29.5] GHz band. The 1 × 4 array features a peak gain of 10.1 dBi. Unless mentioned otherwise, an arbitrary waveform generator (AWG) (92 GSps Keysight M8196a) is used as signal generator to directly generate a modulated 2 GBd QPSK signal with a root-raised cosine transmit filter with a roll-off factor of 0.35 at a carrier frequency of 28 GHz with a peak signal amplitude of $V_{\mathrm{mmWave,p}}$. This signal is taken to showcase the ability of mmWave-over-fiber to distribute a broadband signal that fits in the n257 5G band. Furthermore, the laser (1550-nm BASIC NKT Photonics) output power equals P_{opt}. The MZM (Fujitsu FTM7937EZ $LiNbO_3$, $V_\pi = 3.5$ V) is biased at its quadrature with a benchtop power supply to ensure linear electro-optic conversion. In the current setup, the dc bias is manually adjusted to minimize drift due to RF heating. Yet, in a practical setup, this can automatically be realized by a feedback loop [35]. The MZM is driven in a push (uplink) or push–pull (downlink) configuration to implement optical DSB modulation. A single-mode optical fiber [with standard dispersion of 17 ps/(nm· km)] is used to interconnect RAU to CO. Its length of 20 m is well below the first chromatic-dispersion-induced extinction dip at around 4 km

for a single-carrier (30 GHz) DSB-modulated signal around a 1550-nm light carrier [29]. A commercial photodiode (Finisar XPDV2120R-VF-FA) with a reverse bias voltage of 2 V is used. All the amplifiers in the setup are low-noise amplifiers (Analog Devices HMC1040). Moreover, the RAU and the UE of the setup are installed in an anechoic chamber mimicking free-space conditions, with a separation distance of 2.2 m. The signal, received by the UE's antenna, is amplified and directly sampled by a real-time oscilloscope (RTO) (80 Gsps Keysight DSAZ634a), which also runs the Keysight PathWave VSA 89600 software for fair comparison.

As a starting point, the input parameters of the system-level model, annotated in Fig. 2(b) and (e), are determined by consulting the component's datasheet, performing measurements, or full-wave simulations. The frequency-dependent amplifier gain is measured using a Keysight N5247B PNA-X vector network analyzer (VNA), while its nonlinear distortion parameters are taken from the datasheet. For the mmWave-over-fiber link, the electrical back-to-back scattering parameters and its nonlinear distortion are measured with the VNA for an optical power at the input of the MZM of 13.5 dBm. Simulating this gain at different optical powers is implemented by correcting the measured $|S_{21}|$ as [16]

$$|S_{21,\text{corr}}| = |S_{21}| + 2 \cdot \left(P_{\text{opt}} - 13.5 \text{ dBm}\right) \tag{3}$$

with $|S_{21,\text{corr}}|$ being the corrected electrical gain at optical power P_{opt}. Using an external modulator limits the frequency chirp with respect to a directly modulated laser. Owing to the dc extinction ratio $\geq$20 dB of the adopted Fujitsu laser, the effect of the remaining frequency chirp can be modeled as an additional loss to the dispersion penalty [36]. For our setup, this additional loss is included in the "Gain" building block of the mmWave-over-fiber submodel [Fig. 2(b) and (e)]. Since the optical link varies between up- and downlink in the measurements, this corrected insertion loss can differ by an offset factor. Next, the wireless channel is constructed by simulating the realized gain of the RAU front-end (feeding network with corporate feed and antenna array) and the single element in CST Microwave Studio's frequency-domain solver. Using these realized gain patterns, a wireless channel model is implemented in MATLAB using the Friis power transmission equations, since all the measurements are performed in a (semi-)anechoic environment.

Owing to the modular nature of the simulation suite, more advanced wireless channel models/measurements can be incorporated in the future to optimize RAU placement in real-life environments. In addition, a two-tone measurement is performed to determine the distortion introduced by the AWG and RTO. As initial value for the noise temperature, 290 K is taken. The parameters are then simultaneously optimized for the up- and downlink to account for additional losses in the link, originating from the use of evaluation boards instead of integrated ICs, interconnects, and cables. They are given in Table I. As the table only lists the frequency-dependent parameters at the center frequency of 28 GHz, Fig. 4 shows the amplifier gain, optical link loss, and wireless channel attenuation as a function of frequency.

TABLE I
SYSTEM-LEVEL MODEL PARAMETERS FOR A MMWAVE-OVER-FIBER WIRELESS LINK IN CASE AN ANTENNA ARRAY WITH CORPORATE FEED IS USED AT THE RAU

Amplification: HMC1040	
$Gain^*$ at 28 GHz	23.8 dB
OP_{1dB}	8.5 dBm
OP_{sat}	10.5 dBm
OIP_3	18.5 dBm
NF	2.2 dB
Optical Link	
Att^* at 28 GHz	25.9 dB
IP_{1dB}	5 dBm
IP_{sat}	8 dBm
IIP_3	18.4 dBm
Wireless channel	
Att^* at 28 GHz	55.7 dB
Non-linearity: AWG	
IP_{1dB}	−11 dBm
IP_{sat}	−8 dBm
IIP_3	−3 dBm
Non-linearity: RTO	
IP_{1dB}	−11 dBm
IP_{sat}	−8 dBm
IIP_3	−3.5 dBm
Overall parameters	
T_0	300 K
*: Frequency-dependent	

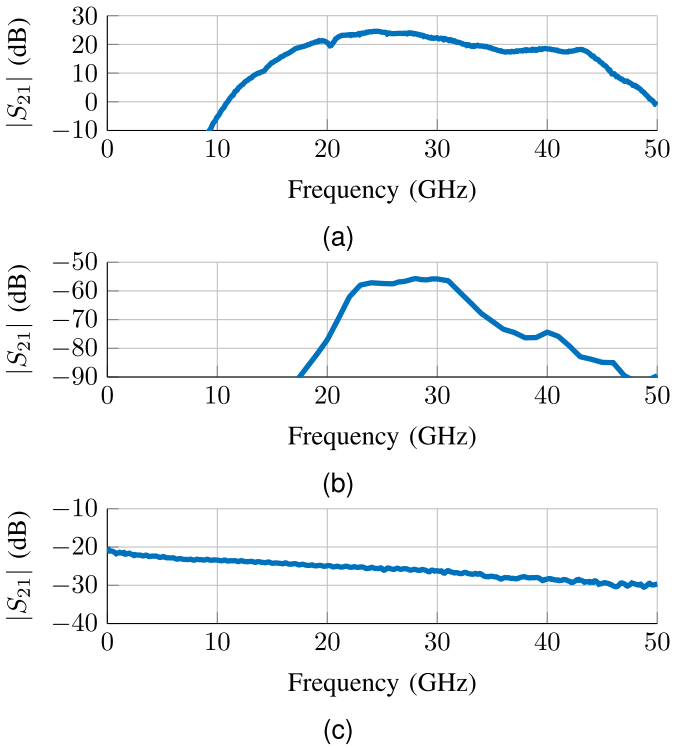

Fig. 4. Frequency-dependent model parameters as a function of the frequency. (a) Amplifier (HMC1040) gain. (b) Wireless channel loss. (c) Optical link loss.

B. First Validation of the Model

Figs. 5–7 show the rms EVM as a function of the mmWave-over-fiber link's optical power, peak signal amplitude, and baud rate, respectively, comparing the simulation and measurement as a validation of the model. These results also

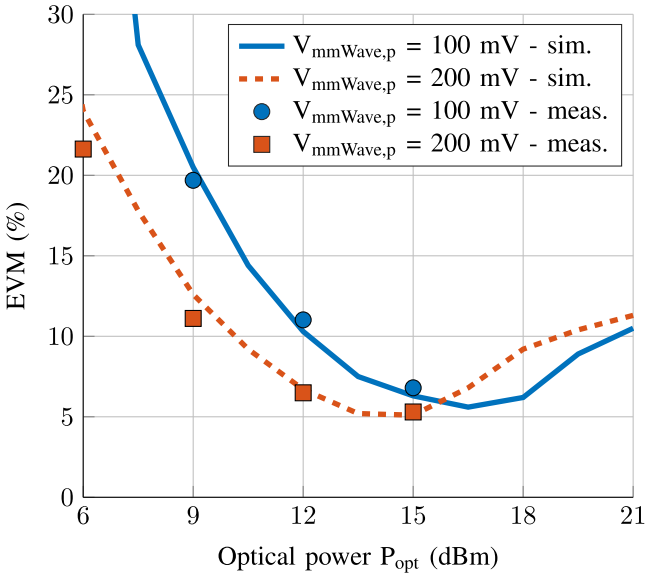

Fig. 5. Measured and simulated rms EVM values as a function of the laser output power.

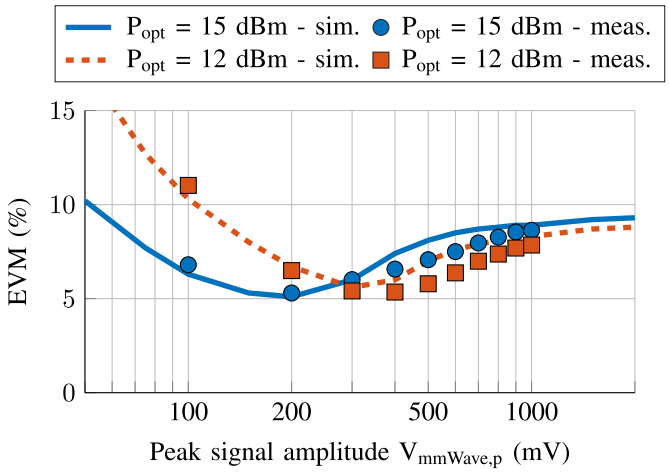

Fig. 6. Simulated and measured rms EVM as a function of the peak of the mmWave signal ($V_{mmWave,p}$) driving the MZM.

illustrate the behavior of the link and explain the choice of these parameters in the remainder of the experiments.

More specifically, Fig. 5 shows the rms EVM as a function of optical laser power for two different AWG output amplitudes ($V_{mmWave,p}$), equal to 100 and 200 mV. For both the values of $V_{mmWave,p}$, the simulations (lines) and measurements (dots) indicate an initial decrease in EVM for increasing optical power and show excellent agreement with a maximum error in EVM of only 0.8% and 2.4% for the 100- and 200-mV traces, respectively. This increase in signal quality is expected since the increased light power does not influence the modulation depth and, therefore, does not increase the MZM-induced nonlinear distortion (1), but only the total modulated power. In our measurement setup, the optical power is limited by the used CO laser's maximum output power of 15 dBm, but in principle, the laser power can be further increased, improving the slope efficiency of the optical modulator [16], and hence decreasing the overall losses in the intrinsic analog radio-over-fiber link. Yet, when predicting the EVM for optical powers beyond 15 dBm, the simulation suite shows that the RAU's amplifiers are driven in compression, giving rise to nonlinear effects and deteriorating signal quality beyond the optimal value. Moreover, comparing the minimum EVM values of both the curves reveals that the optimal value for the 100-mV curve is slightly (0.5%) higher than for the 200-mV curve. This is because a higher optical power gives rise to increased shot noise. Yet, care should be taken that the optical fiber's field intensity remains sufficiently low such that nonlinear effects including Raman scattering remain negligible [37], and the laser's RIN remains sufficiently low [16].

In addition, Fig. 6 depicts the influence of the RF signal power on the UE's signal quality for an optical power of 12 and 15 dBm. The simulation results (lines) agree well with the measurements (dots) with an overall maximum deviation of 1.3% between both. At lower RF power (such as for a peak signal amplitude 100 mV), the received signal is mainly noise-limited, whereas at higher RF power (beyond peak signal amplitude ≈500 mV), nonlinear distortion limits the performance of the system. As also shown in Fig. 6, there is an optimal value for the RF signal power with an optimal tradeoff between noise and nonlinear distortion, which leads to minimum EVM and maximum link performance. The main contributors to the nonlinear distortion at higher RF powers in this setup are the second amplifier in the RAU's optical receive chain and the signal generation in the AWG since its spur-free dynamic range (SFDR) decreases significantly near its Nyquist rate and overall bandwidth. Although the previous experiment showed that a higher optical power generally results in a better signal quality, this analysis shows that a decrease in optical power can be compensated for to a certain degree by an increase in RF power. Since the photocurrent I_{PD} scales linearly with the optical power P_{opt} (2), the photodiode's electrical output power scales quadratically with the optical power. The reduced optical power can be compensated by a quadratic increase in RF power, at the penalty of introducing more nonlinearities in the MZM. Indeed, it can be observed in Fig. 6 that as the laser power decreases by 3 dB, the optimum signal amplitude approximately doubles (400 versus 200 mV).

Finally, Fig. 7 shows the simulated and measured EVMs for different symbol rates at a carrier frequency of 28 GHz for a peak signal amplitude of 200 mV and a laser power of 15 dBm. Again, a good agreement between the simulation and measurement can be observed, indicating a similar trend. A maximum deviation of only 2.4% is observed for baud rates above 4 GBd. This deviation can be mainly attributed to the nonideal behavior of the AWG as a mmWave source and the RTO, both operating close to their operational limits in terms of DAC/ADC sampling rate and analog bandwidth.

These experiments (Figs. 5–7) validate the proposed system-level model of the mmWave-over-fiber wireless link, accurately predicting the measured signal quality when tuning a variety of parameters such as the RF power, optical laser power, and baudrate without reoptimization of the model.

In addition, the model also correctly predicts the most optimal operating point, being a laser power of 15 dBm and

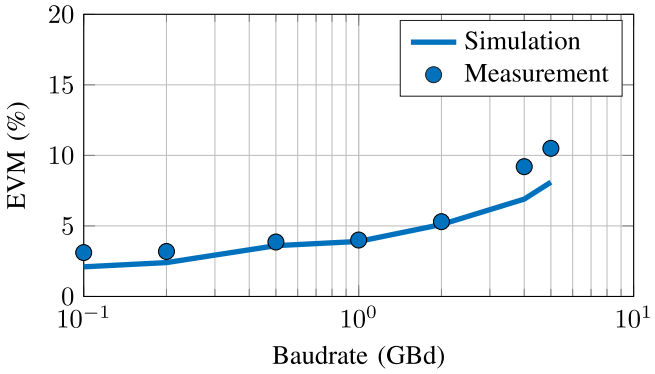

Fig. 7. Simulated and measured link quality as a function of symbol rate.

a signal amplitude of 200 mV, which will be used in the remainder of the experiments.

C. Uplink Versus Downlink

In this section, the downlink and uplink signal quality is studied for a UE located at different locations in an anechoic environment. This allows validating the model for significantly different magnitudes of wireless channel losses and allows predicting the coverage area of an RAU.

In this setup, the RAU and UE are deployed inside an anechoic chamber with a wireless propagation distance of 2.2 m. The RAU is mounted on a rotational stage of an NSI-MI spherical near-field antenna measurement system. By rotating the RAU, the position of the UE with respect to the RAU is varied while keeping the propagation distance constant.

Fig. 8(a) shows the simulated downlink signal quality for a UE positioned at different locations with coordinates (X,Y) in an anechoic room with dimensions 5 m $\times$ 10 m. As expected for a free-space environment, the best signal quality is obtained when the UE is located in the main lobe direction, gradually decreasing as the wireless propagation distance (the path loss) increases. The red area indicates the locations where, according to 3GPP, a data rate of 12 Gb/s (2 GBd with 64-QAM symbols) in the n257 5G band can be achieved.

Fig. 8(b) depicts the measured and simulated rms EVM values as a function of the UE angle θ (defined as the angle between the UE and RAU), for a fixed wireless propagation distance of 2.2 m between RAU and UE, as annotated by the white dotted line in Fig. 8(a). A good agreement between the simulation and measurement is observed and good signal qualities are achieved in the array's main lobe for the downlink. Although a slightly worse measured rms EVM of 5.7% is achieved in the uplink (versus 5.4% in the downlink), the simulation and measurement again agree well. Nevertheless, in both the cases, a discrepancy in signal quality is observed in the sidelobes around θ $\pm$45°C. This can be attributed to the difference in sidelobe level (SLL) between the simulated and the actual antenna array gains in the mmWave-over-fiber setup. While the RAU's antenna array is simulated in free-space stand-alone conditions, the vicinity of the amplifiers and cables at the array's backside in the mmWave-over-FiWi link measurement setup [Fig. 2(c)] gives

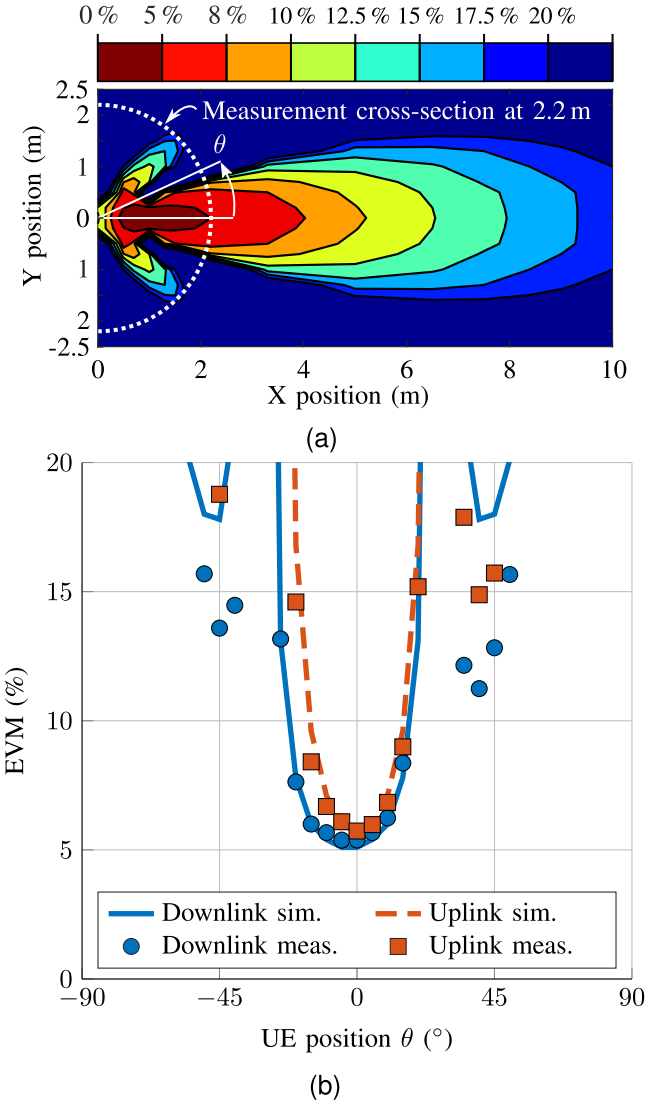

Fig. 8. (a) Simulation of the downlink rms EVM for a UE positioned at different locations in an anechoic room (dimensions: 5 $\times$ 10 m). (b) Comparison between the simulated and measured up- and downlink quality for the indicated cross section [white half-circle in (a)] at a distance 2.2 m.

rise to an increased SLL. Indeed, when an increase in SLL by only 2.5 dB is taken into account in the model, there is a good agreement between the simulated and measured EVM values for all UE positions. To minimize the impact of the integration platform/measurement setup on system-level performance, a higher level of integration should be pursued by integrating all the RAU components at the antenna backside and by adopting an antenna array topology with higher front-to-back ratio, as in [25].

After simulating the RAU and UE antenna system in CST Microwave Studio, the simulation suite requires less than 7 min to generate the downlink curve in Fig. 8(b) with a resolution of 5°, assuming a 5 μs-long 2-GBd QPSK signal (Dell Latitude 5590, CPU: i7-8650U, RAM: 16 GB).

D. Two-Ray Propagation Channel

Next, we focus on the semi-anechoic environment shown in Fig. 9(a). This is realized by deploying a copper sheet in

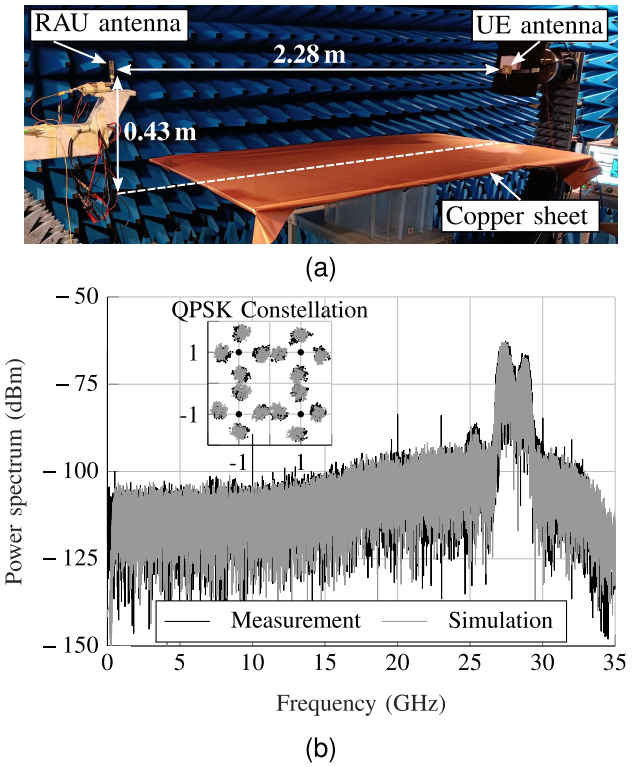

Fig. 9. (a) Measurement setup: a large copper sheet deployed inside the anechoic chamber creates a propagation environment that is well described by the two-ray channel model. (b) Comparison between the simulated and measured spectra of a 2-GBd QPSK signal for a two-ray ground-reflection propagation channel. The inset depicts the simulated and measured constellation plots.

between the RAU and CO to introduce a well-defined ground reflection. The setup can be accurately described by a two-ray channel model. The RAU and UE antenna system are separated by a distance of 2.28 m, both at a height of 0.43 m above the copper plate. As in Section III-B, the mmWave-over-fiber downlink is operated in its optimal working point with a peak voltage amplitude $V_{\mathrm{mmWave,p}}$ of 200 mV and a laser power of 15 dBm.

Fig. 9(b) shows comparison of the measured and simulated spectra at the UE when a 500-ns-long 2-GBd QPSK signal is transmitted. An excellent agreement is observed, with the model not only predicting the frequency at which the direct and ground-reflected waves interfere destructively but also accurately capturing the signal strength of both paths. The figure also compares the simulated and measured constellation plots (4000 symbols). As a result of the multipath propagation, the QPSK symbols deviate from their ideal constellation points [black dots in the inset of Fig. 9(b)] and each point splits up into four distinct point clouds. This behavior is again successfully predicted by the model, providing a first validation of the simulation suite for multipath environments.

IV. Multibeam Antenna Array

The proposed model is further validated by considering an alternative measurement scenario involving a multibeam RAU implementing local beamforming. The setup is identical to the setup as shown in Fig. 1, except that the RAU is now based on a 1 × 4 AFSIW antenna array which is compactly integrated with a low-loss and broadband 4 × 4 Butler matrix implemented in the grounded-coplanar waveguide technology [22]. Through four different connectorized ports, the integrated beamforming array is able to generate four beams in four different discrete directions. The operational frequency band ranges from 23.75 to 31 GHz, and the maximal measured gain equals 12.3 dB.

First, we validate the model by focusing on the case where a single beam is switched to several discrete directions, in the meantime also demonstrating the potential of local beamforming to extend system coverage in a cost-effective way. Next, a multibeam scenario is considered, where the RAU simultaneously serves two UEs in two distinct directions to analyze the influence of residual inter-user interference.

A. Single Beam

Fig. 10 shows the downlink EVM for each of the four input ports of the multibeam RAU as a function of the angle between RAU and UE when the UE is positioned at different locations at a fixed distance of 2.2 m with respect to the RAU. When comparing the simulations (solid lines) with the measurements (dots), a good agreement is noted, especially along the main beams. A small discrepancy can be observed between the simulated and measured beamwidths. Again, the simulated signal quality in the sidelobes is slightly lower than observed during the measurements. This is again due to the difference between the full-wave simulation of the co-designed BFN with antennas and the realized antenna array. Comparing the results of the fixed-beam-based RAU and the multibeam RAU, an identical signal quality is observed when the UE is illuminated by the RAU's main beam, proving both BFNs have comparable insertion losses. Moreover, when comparing the angular sectors covered at an EVM below 8% by the two RAU implementations, it is immediately clear that the multibeam RAU covers a four times larger angular sector, at the cost of requiring an additional RF switch.

B. Impact of Multiple Active Beams

Finally, the model is used to predict the change in signal quality when simultaneously transmitting two beams rather than one, illustrating the capability of the model to incorporate inter-user interference.

This setup now involves two different mmWave-over-fiber links, each driving one of the input ports of the Butler matrix with a different 2-GBd signal (generated with a different length pseudorandom binary sequence (PRBS) generator polynomial to distinguish between both the beams at the receiver by leveraging a custom zero-forcing equalizer in MATLAB). The maximum laser power is now split over the two optical links and the amplitude of the generated signals is 400 mV and 500 mV for Butler matrix ports 3 and 4, respectively. While in this setup, the two mmWave-over-fiber links are used to exchange two distinct signals to a multibeam RAU, they could also be used to serve two RAUs. In the latter case, wavelength division multiplexing could be used to support multiple beams per RAU [38]. The model includes this second mmWave-over-fiber link and takes into account the different MZM

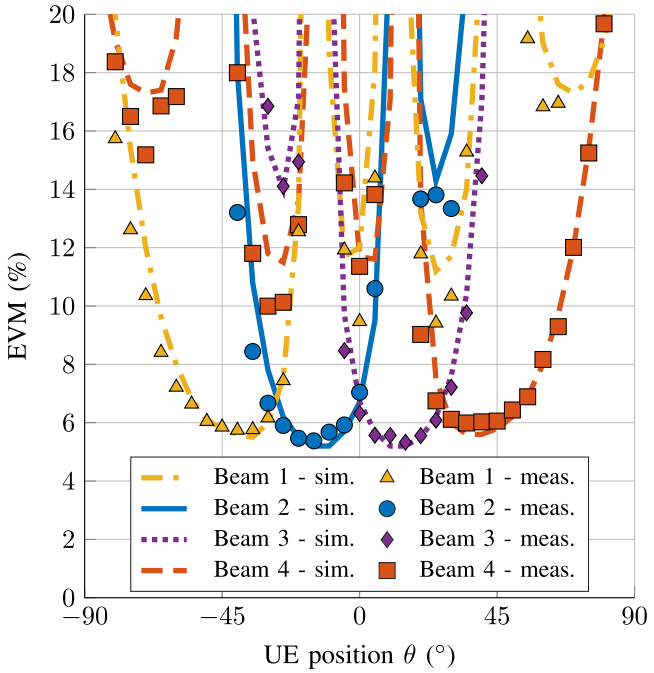

Fig. 10. Simulated (solid) and measured (dots) rms EVM values of a mmWave-over-fiber wireless downlink as a function of UE position in case a switched-beam RAU is used.

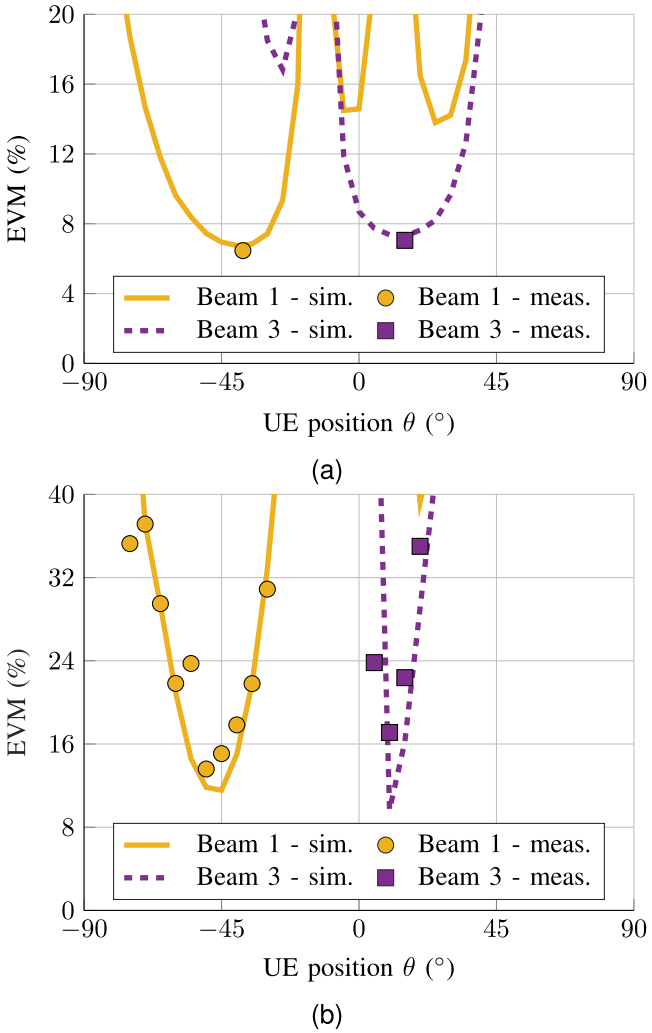

Fig. 11. Simulated (solid) and measured (dashed) rms EVM values as a function of UE position for downlink communication with a multibeam RAU when (a) beam 1 and beam 3 are individually activated and when (b) beam 1 and beam 3 are simultaneously activated.

driving voltages used during the measurements, resulting from slight variations in the mmWave-over-fiber links' equipment. In addition, the full-wave simulation of antenna array with integrated BFN incorporates the BFN's imperfections, such as electromagnetic coupling and insertion losses.

First, the simulated and measured signal qualities are compared when only one of both the links is active. This comparison is shown in Fig. 11(a). These results are comparable to the switched-beam RAU case in Fig. 10. Yet, a slight increase in EVM (0.8% for beam 1 and 1.8% for beam 3 in measurements) is observed as the available laser power per input port is reduced by 3 dB. At broadside, a good agreement is obtained between the measurements and the simulation suite prediction, with a maximum deviation of only 0.3%.

Fig. 11(b) shows the measured and simulated rms EVM values when two beams (beams 1 and 3) are transmitted simultaneously. Again, the measured EVM is predicted well by our simulation suite. Minor deviations can be attributed to the difference in the simulated and actual SLL of the multibeam RAU and to minor phase errors in the manufactured Butler matrix, introducing a shift in the beam pattern nulls. Comparing to Fig. 11(a) reveals that the signal quality deteriorates due to inter-beam interference. In particular, the best EVM is worse when two beams are active and the angular range over which the EVM remains below 17.5% (3GPP criterion for QPSK transmission) is smaller. The latter effect is more pronounced for beam 3 as the side lobes of beam 1 are higher within the half-power beamwidth of beam 3 [as seen in Fig. 11(a)].

The time required by the simulation suite to calculate the EVM for all UE positions in Fig. 11(b) (with a resolution of 5°) remains below 12 min for two simultaneous mmWave-over-fiber wireless links, assuming a transmitted 5 μs-long 2-GBd QPSK signal (compared with 7 min for a single mmWave-over-fiber link in Section III; Dell Latitude 5590, CPU: i7-8650U, RAM: 16 GB).

V. Conclusion

We have proposed a dedicated simulation suite to predict the system-level performance of mmWave-over-fiber-based DASs. Specifically, the simulation suite incorporates accurate models for the mmWave-over-fiber link and the electronic amplifiers, including nonlinear distortion and noise, full-wave models for the antenna front-ends, capturing the most important electromagnetic effects, and analytical wireless channel models, accounting for the high propagation losses encountered at mmWave frequencies.

A thorough validation was performed by means of an extensive measurement campaign on a representative FiWi link, supporting both up- and downlink communication. First, we have focused on a single mobile user served by a fixed-beam RAU, interconnected to the CO by means of a single mmWave-over-fiber link, in free-space conditions. The

up/downlink's rms EVM was accurately predicted over a wide range of user positions and system parameters. In addition, the impact of a two-ray ground-reflection channel on signal quality was analyzed to prove the simulation suite's versatility. Next, a more complex scenario was considered where a multibeam RAU simultaneously serves two mobile users by means of two independent mmWave-over-fiber links. Again, good agreement between the simulation and measurement was obtained, proving that inter-user interference is accurately captured.

In the future, the simulation suite can be further extended with more advanced channel models, by, for instance, also including ray-tracing-based simulators, and it may be further validated by larger multi-RAU measurement campaigns. In addition, the proposed model can be used to test various calibration and channel estimation algorithms, as well as taking a step toward dynamic link budgeting, thereby becoming a very powerful tool in planning the deployment of a DAS and optimizing the configuration of its RAUs, the CO architecture, and the signal processing toward the target application, the wireless propagation environment, and the number of expected users.

REFERENCES

[1] M. Giordani et al., "Toward 6G networks: Use cases and technologies," *IEEE Commun. Mag.*, vol. 58, no. 3, pp. 55–61, Mar. 2020.

[2] A. Moerman et al., "Beyond 5G without obstacles: mmWave-over-fiber distributed antenna systems," *IEEE Commun. Mag.*, vol. 60, no. 1, pp. 27–33, Jan. 2022.

[3] E. Björnson, Ö. Özdogan, and E. G. Larsson, "Reconfigurable intelligent surfaces: Three myths and two critical questions," *IEEE Commun. Mag.*, vol. 58, no. 12, pp. 90–96, Dec. 2020.

[4] J. Rao et al., "A novel reconfigurable intelligent surface for wide-angle passive beamforming," *IEEE Trans. Microw. Theory Techn.*, vol. 70, no. 12, pp. 5427–5439, Dec. 2022.

[5] M. Di Renzo et al., "Smart radio environments empowered by reconfigurable intelligent surfaces: How it works, state of research, and the road ahead," *IEEE J. Sel. Areas Commun.*, vol. 38, no. 11, pp. 2450–2525, Nov. 2020.

[6] I. C. Sezgin et al., "A low-complexity distributed-MIMO testbed based on high-speed sigma-delta-over-fiber," *IEEE Trans. Microw. Theory Techn.*, vol. 67, no. 7, pp. 2861–2872, Jul. 2019.

[7] H. Q. Ngo, A. Ashikhmin, H. Yang, E. G. Larsson, and T. L. Marzetta, "Cell-free massive MIMO versus small cells," *IEEE Trans. Wireless Commun.*, vol. 16, no. 3, pp. 1834–1850, Mar. 2017.

[8] S. Hu, F. Rusek, and O. Edfors, "Beyond massive MIMO: The potential of data transmission with large intelligent surfaces," *IEEE Trans. Signal Process.*, vol. 66, no. 10, pp. 2746–2758, May 2018.

[9] A. Moerman et al., "mmWave-over-Fiber distributed antenna systems for reliable multi-Gbps wireless communication," in *Proc. URSI AT-AP-RASC*, Gran Canaria, Spain, May 2022, pp. 1–4.

[10] C. Lim et al., "Fiber-wireless networks and subsystem technologies," *J. Lightw. Technol.*, vol. 28, no. 4, pp. 390–405, Feb. 2010.

[11] C.-Y. Wu et al., "Distributed antenna system using sigma-delta intermediate-frequency-over-fiber for frequency bands above 24 GHz," *J. Lightw. Technol.*, vol. 38, no. 10, pp. 2765–2773, May 15, 2020.

[12] L. Bogaert et al., "SiPhotonics/GaAs 28-GHz transceiver with reflective EAM for laser-less mmWave-over-fiber," *J. Lightw. Technol.*, vol. 39, no. 3, pp. 779–786, Feb. 1, 2021.

[13] C. Fager, T. Eriksson, F. Barradas, K. Hausmair, T. Cunha, and J. C. Pedro, "Linearity and efficiency in 5G transmitters: New techniques for analyzing efficiency, linearity, and linearization in a 5G active antenna transmitter context," *IEEE Microw. Mag.*, vol. 20, no. 5, pp. 35–49, May 2019.

[14] C.-X. Wang, J. Bian, J. Sun, W. Zhang, and M. Zhang, "A survey of 5G channel measurements and models," *IEEE Commun. Surveys Tuts.*, vol. 20, no. 4, pp. 3142–3168, 4th Quart., 2018.

[15] J. L. Corral, J. Marti, and J. M. Fuster, "General expressions for IM/DD dispersive analog optical links with external modulation or optical up-conversion in a Mach–Zehnder electrooptical modulator," *IEEE Trans. Microw. Theory Techn.*, vol. 49, no. 10, pp. 1968–1976, Oct. 2001.

[16] C. H. Cox, III, E. I. Ackerman, G. Betts, and J. L. Prince, "Limits on the performance of RF-over-fiber links and their impact on device design," *IEEE Trans. Microw. Theory Techn.*, vol. 54, no. 2, pp. 906–920, Feb. 2006.

[17] M. U. Hadi, H. Jung, S. Ghaffar, P. A. Traverso, and G. Tartarini, "Optimized digital radio over fiber system for medium range communication," *Opt. Commun.*, vol. 443, pp. 177–185, Jul. 2019.

[18] Y. Tian, K.-L. Lee, C. Lim, and A. Nirmalathas, "60 GHz analog radio-over-fiber fronthaul investigations," *J. Lightw. Technol.*, vol. 35, no. 19, pp. 4304–4310, Oct. 1, 2017.

[19] J. James, P. Shen, A. Nkansah, X. Liang, and N. J. Gomes, "Nonlinearity and noise effects in multi-level signal millimeter-wave over fiber transmission using single and dual wavelength modulation," *IEEE Trans. Microw. Theory Techn.*, vol. 58, no. 11, pp. 3189–3198, Nov. 2010.

[20] C. Vagionas et al., "Linearity measurements on a 5G mmWave fiber wireless IFoF fronthaul link with analog RF beamforming and 120° degrees steering," *IEEE Commun. Lett.*, vol. 24, no. 12, pp. 2839–2843, Dec. 2020.

[21] A. Moerman et al., "System-level model for mmWave-over-fiber distributed antenna systems," in *Proc. IEEE PAST*, Waltham, MA, USA, Oct. 2022, pp. 1–4.

[22] L. Van Messem et al., "A 4×4 millimeterwave-frequency Butler matrix in grounded co-planar waveguide technology for compact integration with 5G antenna arrays," *IEEE Trans. Microw. Theory Techn.*, vol. 71, no. 1, pp. 122–134, Jan. 2023.

[23] L. Breyne, G. Torfs, X. Yin, P. Demeester, and J. Bauwelinck, "Comparison between analog radio-over-fiber and sigma delta modulated radio-over-fiber," *IEEE Photon. Technol. Lett.*, vol. 29, no. 21, pp. 1808–1811, Nov. 1, 2017.

[24] I. Lima de Paula et al., "Cost-effective high-performance air-filled SIW antenna array for the global 5G 26 GHz and 28 GHz bands," *IEEE Antennas Wireless Propag. Lett.*, vol. 20, no. 2, pp. 194–198, Feb. 2021.

[25] I. Lima de Paula et al., "Air-filled SIW remote antenna unit with true time delay optical beamforming for mmWave-over-fiber systems," *J. Lightw. Technol.*, vol. 40, no. 20, pp. 6961–6975, Oct. 15, 2022.

[26] Q. Zhang et al., "Two-dimensional phased-array receiver based on integrated silicon true time delay lines," *IEEE Trans. Microw. Theory Techn.*, vol. 71, no. 3, pp. 1251–1261, Mar. 2023, doi: 10.1109/TMTT.2022.3214482.

[27] U. Gliese, K. Colladay, A. S. Hastings, D. A. Tulchinsky, V. J. Urick, and K. J. Williams, "RF power conversion efficiency of photodiodes driven by Mach–Zehnder modulators," *IEEE Trans. Microw. Theory Techn.*, vol. 58, no. 11, pp. 3359–3371, Nov. 2010.

[28] T. Young, J. Conradi, and W. R. Tinga, "Generation and transmission of FM and $\pi/4$ DQPSK signals at microwave frequencies using harmonic generation and optoelectronic mixing in Mach–Zehnder modulators," *IEEE Trans. Microw. Theory Techn.*, vol. 44, no. 3, pp. 446–453, Mar. 1996.

[29] U. Gliese, S. Norskov, and T. N. Nielsen, "Chromatic dispersion in fiber-optic microwave and millimeter-wave links," *IEEE Trans. Microw. Theory Techn.*, vol. 44, no. 10, pp. 1716–1724, Oct. 1996.

[30] H. Shams, P. M. Anandarajah, P. Perry, and L. P. Barry, "Optical generation of modulated millimeter waves based on a gain-switched laser," *IEEE Trans. Microw. Theory Techn.*, vol. 58, no. 11, pp. 3372–3380, Nov. 2010.

[31] K. Y. Kapusuz, A. V. Berghe, S. Lemey, and H. Rogier, "Partially filled half-mode substrate integrated waveguide leaky-wave antenna for 24 GHz automotive radar," *IEEE Antennas Wireless Propag. Lett.*, vol. 20, no. 1, pp. 33–37, Jan. 2021.

[32] C. H. Cox, "Noise in links," in *Analog Optical Links: Theory and Practice*. Cambridge, U.K.: Cambridge Univ. Press, 2004, ch. 5, sec. 2, pp. 160–168.

[33] Y. Yang, C. Lim, and A. Nirmalathas, "Multichannel digitized RF-over-fiber transmission based on bandpass sampling and FPGA," *IEEE Trans. Microw. Theory Techn.*, vol. 58, no. 11, pp. 3181–3188, Nov. 2010.

[34] *LTE; Evolved Universal Terrestrial Radio Access (E-UTRA); Base Station (BS) Radio Transmission and Reception—Release 15—V15.3.0*, document TR 36.104, 3GPP, Jan. 2021. Accessed: Jan. 2023. [Online]. Available: https://www.3gpp.org/dynareport/36-series.htm

[35] Y. Li, Y. Zhang, and Y. Huang, "Any bias point control technique for Mach–Zehnder modulator," *IEEE Photon. Technol. Lett.*, vol. 25, no. 24, pp. 2412–2415, Dec. 15, 2013.

[36] S. Walklin and J. Conradi, "Effect of Mach–Zehnder modulator DC extinction ratio on residual chirp-induced dispersion in 10-Gb/s binary and AM-PSK duobinary lightwave systems," *IEEE Photon. Technol. Lett.*, vol. 9, no. 10, pp. 1400–1402, Oct. 1997.
[37] R. H. Stolen, "Nonlinearity in fiber transmission," *Proc. IEEE*, vol. 68, no. 10, pp. 1232–1236, Oct. 1980.
[38] E. Ruggeri et al., "A 5G fiber wireless 4Gb/s WDM fronthaul for flexible 360° coverage in V-band massive MIMO small cells," *J. Lightw. Technol.*, vol. 39, no. 4, pp. 1081–1088, Feb. 15, 2021.

Arno Moerman (Student Member, IEEE) received the M.Sc. degree from Ghent University, Ghent, Belgium, in 2019.

He is currently a Ph.D. Researcher with Ghent University/imec. His research interests are antenna systems for future generation mobile communication networks.

Olivier Caytan (Member, IEEE) received the M.Sc. and Ph.D. degrees in electrical engineering from Ghent University, Ghent, Belgium, in 2014 and 2019, respectively.

He is currently a Post-Doctoral Researcher with the Electromagnetics Group, Department of Information Technology, Ghent University/imec. His research interests include microwave engineering and active antenna systems, in particular mm-wave opto-electronic antenna systems for 5G and beyond.

Laura Van Messem (Student Member, IEEE) received the M.Sc. degree in electrical engineering from Ghent University/imec, Ghent, Belgium, in 2019, where she is currently pursuing the Ph.D. degree in electrical engineering at the IDLab-Electromagnetics Group, Department of Information Technology (INTEC).

Her research interests include next-generation communication systems, more specifically highly efficient millimeter-wave and THz passive solutions.

Joris Van Kerrebrouck (Member, IEEE) is currently a Post-Doctoral Researcher with the IDLab- Design Group, Ghent University/imec, Ghent, Belgium. His research interests include optical communication and radio over fiber (RoF) for 5G applications.

Guy Torfs (Senior Member, IEEE) received the Engineering degree in applied electronics and the Ph.D. degree in applied sciences and electronics from Ghent University, Ghent, Belgium, in 2007 and 2012, respectively.

Since 2011, he has been with Ghent University/imec, where he became an Assistant Professor in 2015. His current research interests focused on high-speed mixed-signal designs for wireless baseband and fiber-optic and backplane communication systems, including digital signal processing and calibration, analog equalization circuits, and clock and data recovery systems.

Dr. Torfs was a co-recipient of the 2015 DesignCon Best Paper Award in the High-Speed Signal Design Category and the European Conference on Optical Communication (ECOC) 2019 Best Demo Award. In 2014, as part of the Bi-PON and Cascaded Bi-PON Team, he was rewarded with the Greentouch 1000× Award. He has serves as an Associate Editor for IEEE TRANSACTIONS ON CIRCUITS AND SYSTEMS—II: EXPRESS BRIEFS.

Piet Demeester (Fellow, IEEE) is currently a Professor with Ghent University, Ghent, Belgium, and the Director of the IDLab, imec Research Group, UGent. The IDLab's research activities include distributed intelligence in the IoT, machine learning and data mining, semantic intelligence, cloud and big data infrastructures, fixed and wireless networking, electromagnetics, and high-frequency circuit design. He holds the Advanced ERC Grant.

Hendrik Rogier (Senior Member, IEEE) received the Electrical Engineering and Ph.D. degrees from Ghent University, Ghent, Belgium, in 1994 and 1999, respectively.

From October 2003 to April 2004, he was a Visiting Scientist with the Mobile Communications Group, Vienna University of Technology, Vienna, Austria. He is currently a Senior Full Professor with the Department of Information Technology, Ghent University, and a Guest Professor with the Interuniversity Microelectronics Centre, Ghent. He has authored or coauthored about 200 articles in international journals and about 220 contributions in conference proceedings. His current research interests are antenna systems, radiowave propagation, body-centric communication, numerical electromagnetics, electromagnetic compatibility, and power/signal integrity.

Dr. Rogier was twice awarded the International Union of Radio Science (URSI) Young Scientist Award. Moreover, he received the 2014 Premium Award for Best Paper in *IET Electronics Letters* and several awards at conferences. From 2017 to 2019, he was an Associate Editor of IEEE TRANSACTIONS ON MICROWAVE THEORY AND TECHNIQUES. He is also an Associate Editor of the *IET Electronics Letters* and the *IET Microwaves, Antennas and Propagation*. He acts as the URSI Commission B representative for Belgium.

Sam Lemey (Member, IEEE) received the M.Sc. degree in electronic engineering from Howest University College West Flanders, Kortrijk, Belgium, in 2012, and the Ph.D. degree in electrical engineering from Ghent University, Ghent, Belgium, in 2016.

From January to March 2018, he was a Visiting Scientist with the Terahertz Photonics Group, Institute of Electronics, Microelectronics and Nanotechnology (IEMN), University Lille Nord de France, Lille, France. He is currently a Professor with the Department of Information Technology (INTEC), Ghent University/imec. His research interests include antenna systems for wearable applications, active antenna design for the Internet of Things and (beyond) 5G applications, (opto-electronic) millimeter-wave multiantenna systems, impulse-radio ultra-wideband antenna systems for centimeter-precision localization, and full-wave/circuit co-optimization frameworks to realize (opto-electronic) active (multi-)antenna systems.

Dr. Lemey received the International Union of Radio Science (URSI) Young Scientist Award at the 2020 URSI General Assembly and was awarded the Best Paper Award at the 2016 IEEE Microwave Theory and Technology Society (MTT-S) Topical Conference on Wireless Sensors and Sensor Networks. He was also a co-recipient of the 2015 Best Paper Award at the 22nd IEEE Symposium on Communications and Vehicular Technology in the Benelux and the 2019 European Conference on Optical Communication (ECOC) Best Demo Award.